Aqueous Zn-Ion Batteries Hot Paper

How to cite:
International Edition: doi.org/10.1002/anie.202300125
German Edition: doi.org/10.1002/ange.202300125

Integrated Micro Space Electrostatic Field in Aqueous Zn-Ion Battery: Scalable Electrospray Fabrication of Porous Crystalline Anode Coating

Can Guo[+], Jie Zhou[+], Yuting Chen[+], Huifen Zhuang, Jie Li, Jianlin Huang, Yuluan Zhang, Yifa Chen, Shun-Li Li, and Ya-Qian Lan**

Abstract: The inhomogeneous consumption of anions and direct contact between electrolyte and anode during the Zn-deposition process generate Zn-dendrites and side reactions that can aggravate the space-charge effect to hinder the practical implementation of zinc-metal batteries (ZMBs). Herein, electrospray has been applied for the scalable fabrication ($>10000\,cm^2$ in a batch-experiment) of hetero-metallic cluster covalent-organic-frameworks (MCOF-Ti_6Cu_3) nanosheet-coating (MNC) with integrated micro space electrostatic field for ZMBs anode protection. The MNC@Zn symmetric cell presents ultralow overpotential (≈ 72.8 mV) over 10000 cycles at 1 mAh cm^{-2} with 20 mA cm^{-2}, which is superior to bare Zn and state-of-the-art porous crystalline materials. Theoretical calculations reveal that MNC with integrated micro space electrostatic field can facilitate the deposition-kinetic and homogenize the electric field of anode to significantly promote the lifespan of ZMBs.

Introduction

The ever-growing demands for renewable energy storage encourage the eagerness of researchers to investigate reliable, environmentally friendly, and low-cost electrochemical energy storage systems (EESs).[1] Zinc-metal batteries (ZMBs) has been widely recognized as the most promising EES among all available candidates owing to its appealing features including abundant resources, environmental benignity, high specific capacity (820 mAh g^{-1}), low electrochemical potential (−0.762 V vs the standard hydrogen electrode), low toxicity, and intrinsic safety in the air.[1b,2] Since bivalent zinc ions have a significantly stronger and tighter solvation sheath around the exterior than monovalent lithium or sodium ions, they suffer from severely sluggish kinetic entering the electrode host.[3] Specifically, Zn^{2+} prefers to constantly deposit on tip sites of protuberances with the considerably higher electric field that can serve as charge center, which results in severe Zn dendrite growth and aggravates the process over time.[4] Furthermore, the persistent growth of Zn dendrites can generate a mass of "dead Zn" that might accelerate the side reactions owing to excessive exposure between the electrolyte and Zn anode and even pierce the separator, which would result in poor Coulombic efficiency (CE) and cyclability as well as insufficient Zn utilization.[2b,3a] Beyond that, the required substantial desolvation energy around the tips and significant free water concentration at the interface may both initiate the hydrogen evolution reaction and Zn corrosion at the same time.[5] Therefore, it is crucial to create strategies for protecting Zn anode from undesirable Zn deposition and dendrites. Recently, some advancements have been developed around the whole system, including the construction of three-dimensional conductive hosts,[4a,6] the optimization of the electrolyte composition,[7] the formation of metal/zinc alloy,[8] or interfacial modification,[9] etc. Concerning the viability and practicability, a more straightforward and effective interfacial modification strategy for high performance ZMBs would be the design of artificial protective coating to ameliorate less contact with water and uniform distribution of the space electrostatic field for dendrite-free Zn anode.

To this end, the construction of an artificial protective coating with desired space electrostatic field effect, especially that can be rationally designed or well-tuned at the microscopic molecular level (also denoted as micro space electrostatic field), might be of significance for continuously suppressing the dendrite growth and hydrogen evolution reaction for ZMBs.[10] To design the coating with micro space electrostatic field, it would set stringent requirements for the selection of materials. Crystalline materials with well-defined structures and uniformly distributed construction struts might serve as promising candidates to develop integrated micro space electrostatic field system to effectively optimize electric field distribution and Zn deposition as well as elevate the lifespan of ZMBs.[11] Meanwhile, unique functions like hetero-metallic or zincophilic sites that can possibly induce micro space electrostatic field are also much desired for the material design.[4b,11c] With these considerations in mind, covalent organic frameworks (COFs) as a kind of porous crystalline materials with

[*] Dr. C. Guo,[+] J. Zhou,[+] Y. Chen,[+] H. Zhuang, J. Li, J. Huang, Y. Zhang, Prof. Y. Chen, Prof. S.-L. Li, Prof. Y.-Q. Lan
School of Chemistry, South China Normal University
Guangzhou, 510006 (P. R. China)
E-mail: chyf927821@163.com
yqlan@m.scnu.edu.cn
Homepage: http://www.yqlangroup.com/

[+] These authors contributed equally to this work.

fascinating physicochemical properties including high porosity, structural tunability, tunable metal sites, light-weight, and high chemical stability, come to our mind and hold much potential in constructing protective coating with integrated micro space electrostatic field for Zn anode.[12] During past years, some COFs examples have been applied as functional materials to regulate the Zn diffusion, nucleation, and deposition behaviors of ZMBs, for the sake of achieving reversible Zn plating/stripping with dendrite-free morphology.[12a–e] Nevertheless, related works that focus on the construction of integrated micro space electric field systems based on hetero-metallic COFs have been rarely reported as far as we know. Beyond that, the fabrication strategies of COFs for Zn anode protection coating/layer are mainly in situ growth COFs on the Zn anode surface, ex situ COFs casting with polymers or direct COF-membrane pasting induced by solvents.[12a–e] However, in situ growth strategy suffers from an uneven surface caused by uncontrollable reaction rate and complicated synthesis methods of COFs, which is generally hard in the continuous syntheses of large-scale and defect-free COFs based protective layer/coating.[12a] Meanwhile, ex situ COFs casting with polymers or direct COF-membrane pasting methods still face the bottlenecks of pore blockage/compatibility problems caused by polymers or lacking in interfacial interaction with Zn anode surface.[13] Based on the above considerations and inspired by these pioneering works, we intend to apply the electrospray technique for the scalable fabrication of hetero-metallic COFs nanosheet based anode coating with integrated micro space electrostatic field owing to the following considerations: 1) Hetero-metallic COFs with designable structure counterparts might induce integrated micro space electrostatic field to facilitate the deposition kinetics and induce uniform electric field distribution;[4b,11] 2) Electrospray has proven to be a kind of advanced coating technique due to its high production speed, scalable and continuous processing;[11a,14] and 3) COFs in nanosheet forms can make full use of the Zn ion adsorption sites and possess strong interfacial interaction with the Zn anode surface to produce highly homogeneous interface coating through the electrospray technology.[11a,13c,14,15] Thus, hetero-metallic COFs nanosheet with integrated micro space electrostatic field that can be facilely fabricated as Zn anode coating through powerful electrospray method might meet the strict requirements of ZMBs for further anode protection applications, yet related research works have been rarely reported as far we know.

As a proof-of-concept, a hetero-metallic cluster COF-Ti_6Cu_3 (constructed with $\mathbf{Ti_6}$ and $\mathbf{Cu_3}$ clusters) nanosheet (denoted as MNC) with integrated micro space electrostatic field has been successfully designed and applied as a versatile functional interfacial coating for ZMBs anode by large-scale electrospray fabrication ($>10000\ cm^2$ in a batch-experiment) (Scheme 1). MCOF-Ti_6Cu_3 has been pre-exfoliated into nanosheets and fabricated through the electrospray method to prepare MNC on Zn anode. The integrated micro space electrostatic field of MNC with largely improved deposition kinetics can not only homogenize Zn

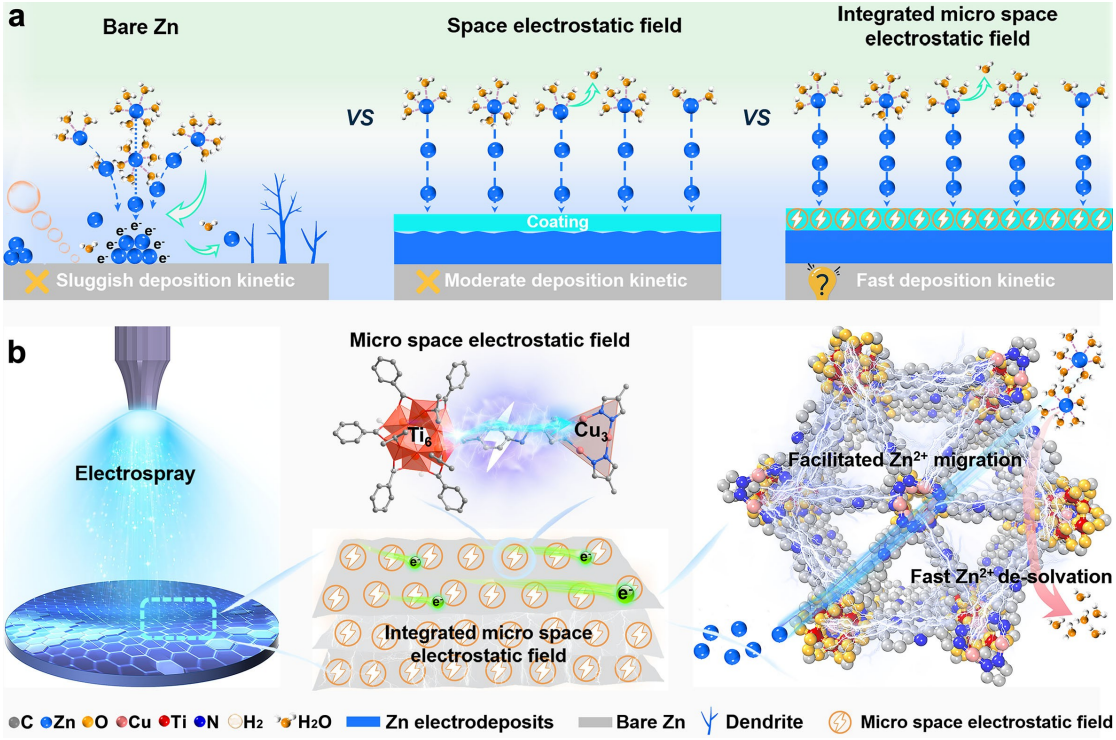

Scheme 1. Schematic illustration of the electrospray fabrication of MNC with integrated micro space electrostatic field for ZMBs Zn coating. (a) The Schematic illustration of the effect of integrated micro space electrostatic field on Zn anode protection coating. (b) The Schematic illustration of electrospray fabrication of MNC with integrated micro space electrostatic field.

deposition and prevent Zn dendrite growth, but also inhibit hydrogen evolution and alleviate Zn erosion stem from blocking the contact between H_2O and the Zn anode surface, which can be proved by the in situ optical microscope results and theoretical calculations. Specifically, the MNC@Zn symmetric cell provide superior Zn plating/stripping behaviors over 10000 cycles and lower the nucleation overpotential of ≈72.8 mV at 1 mAh cm^{-2} with 20 mA cm^{-2}, which is far superior to bare Zn or monomers symmetric cells and represented to be optimal in COF based coatings. Remarkably, MNC@Zn//MnO_2 full cells present the higher long-term cycling stability during 1000 cycles at 2 A g^{-1} and rate performance than that of the bare Zn//MnO_2 full cells. This work affords a new mindset that elaborate porous crystalline Zn anode coating design for constructing high performance aqueous ZMBs that can be readily realized by large-scale electrospray fabrication, which might promote the development of next-generation aqueous battery systems.

Results and Discussion

MNC@Zn (COFs loading, ≈0.02 mg cm^{-2}) is fabricated through the scalable electrospray technique on the commercial Zn foil based on the well-dispersed MCOF-Ti_6Cu_3 nanosheet aqueous suspension (Scheme 1, Figures 1 and detail see Methods). Specifically, it enables large-area fabrication and >10000 cm^2 MNC@Zn can be facilely prepared in a batch-experiment. To prepare the MNC@Zn, the MCOF-Ti_6Cu_3 nanosheet has been firstly characterized (Figure 1). The powder X-ray diffraction (PXRD) pattern of MCOF-Ti_6Cu_3 nanosheet is consistent with the reported one (Figure S1, detail see Methods).[15] Besides, it can be observed from the Fourier-transform infrared spectra that the obvious disappearances of the N–H (3200–3500 cm^{-1}) stretching vibration and C=O (1685 cm^{-1}) peaks are classified as the precursors of $Ti_6O_6(OiPr)_6(AB)_6$ (denoted as **Ti_6**) and $Cu_3(PyCA)_3$ (denoted as **Cu_3**), respectively, indicating the condensation reaction occurs between the two precursors (Figure S2). What's more, a new characteristic peak of the C=N bond appears at 1625 cm^{-1}, which is favorable evidence for forming an imine-linked network.[16] Furthermore, the transmission electron microscopy (TEM) images of MNC show a uniform nanosheet morphology (Figure 1b), which is slightly different from the Ti_6 or Cu_3 cluster nanosheet (Figures S3 and S4). The high crystallinity of MCOF-Ti_6Cu_3 nanosheet is distinctly revealed by the high-resolution TEM test (Figure S5). Thus, a kind of MCOF-Ti_6Cu_3 nanosheet with thickness of ≈4.81 nm can be easily obtained after high frequency ultrasound treatment as detected by the atomic force microscope (AFM) image (Figure 1c). Besides, the surface area and porosity of MCOF-Ti_6Cu_3 nanosheet are evaluated by N_2 adsorption-desorption measurements at 77 K (Figure S6). The sample shows a Brunauer–Emmett–Teller surface area of 152 m^2 g^{-1} and the pore size distribution centered at ≈2.3 nm (Figure S6b).[16a,17] In addition, X-ray photoelectron spectroscopy (XPS) analyses of Ti_6Cu_3 nanosheet, Ti_6 and Cu_3 cluster

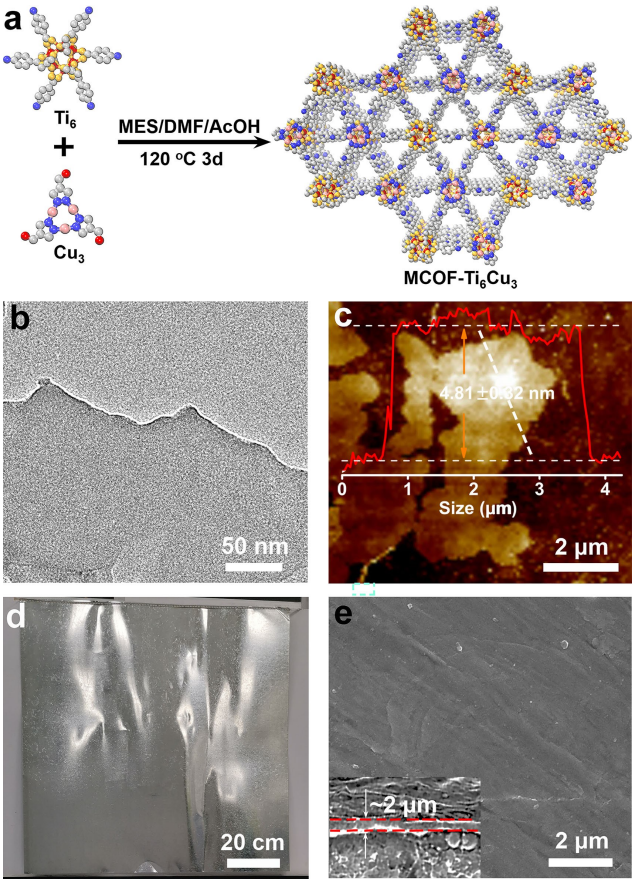

Figure 1. Characterization of MCOF-Ti_6Cu_3 nanosheet and MNC@Zn. (a) Schematic representation of the synthesis and structure of MCOF-Ti_6Cu_3 by the condensation of Ti_6 and Cu_3 clusters. (b) TEM image of MCOF-Ti_6Cu_3 nanosheet. (c) AFM image of MCOF-Ti_6Cu_3 nanosheet. (d) Photograph image of MNC@Zn anode in large-area fabrication (10000 cm^2) in a batch experiment. (e) Top and side view SEM images of MNC@Zn anode (insert is the side view image).

reveal that the Ti 2p binding energy at 459.0 eV of Ti_6 has been compatible with Ti^{4+}, while the Cu 2p binding energies at 932.8 eV and 934.6 eV of Cu_3 can be attributed to Cu^{1+} and Cu^{2+}, respectively (Figures S7 and S8).[16a,17] According to previous studies, Cu^{2+} is produced by surface oxidation, and the Cu valence can be changed from Cu^{1+} to Cu^{2+} without altering the structure of $Cu_3(PyCA)_3$ triangular SBUs.[16a,18] Meanwhile, the XPS spectra of the C, N, and O elements are displayed (Figures S9–S11). For MCOF-Ti_6Cu_3 nanosheet, the creation of built-in electric field and successful covalent bond connection between the two precursors have been confirmed by a negative shift of the Ti 2p binding energy of 0.4 eV and a positive shift of the Cu 2p binding energy of 0.7 eV (Figure S8).[19]

Based on the preparation of MNC, we further fabricate the MNC@Zn with electrospray technique and characterized. The chemical compositions of the obtained samples have been investigated by PXRD measurement. The MNC@Zn obtained through the electrospray fabrication shows obvious peaks matching well with that of MCOF-Ti_6Cu_3 and other typical diffraction peaks of Zn (JCPDS

No. 87-0713) in the PXRD tests (Figure S12). The scanning electron microscopy (SEM) images of MNC@Zn show a dense coating on the surface of Zn foil (Figure 1e). According to the cross-section SEM image, the thickness of the MNC on the Zn foil surface is ≈2 μm (Figure 1e, insert). Most significantly, the tightly coating with a distinctive COF porous architecture is analogous to an artificially constructed sieve, in which it can afford abundant nanopores to serve as ion transport tunnels and further direct the uniform Zn deposition rate across the whole surface of Zn foil. In addition, the polar functional groups of the coating can significantly improve the hydrophilic surface affinity of bare Zn foil (Figure S13).

Based on the above-mentioned results, the more direct evidence of Zn deposition process has been monitored by in situ optical microscopy in real-time using the transparent symmetric cell at the current density of 20 mA cm^{-2} in 1 M $ZnSO_4$ electrolyte (Figures 2a and 2b).[12d,19] The MNC@Zn anode delivers a smooth surface without any hydrogen formation and negligible changes have been observed (Figure 2a). In contrast, some visible protrusions appear on the bare Zn anode surface after 10 cycles during the same plating process and gradually turn into the uncontrolled Zn dendrites (Figure 2b).[12b] This further demonstrates that MNC has an obvious effect on inhibiting Zn dendrite growth and hydrogen evolution to achieve more uniform Zn nucleation and improve the kinetic properties of the batteries. To verify the superiority of the MNC, we track the Zn deposition behaviors of MNC@Zn and bare Zn symmetric cells by ex situ SEM characterizations. The MNC@Zn surface presents a flat and smooth surface after the Zn plating at various current densities of 1, 2, and 3 mA cm^{-2} (Figures 2c–e). By sharp contrast, the bare Zn anode exhibits a rough surface with some protuberance and Zn nanosheets when the current density is at 1 mA cm^{-2} with a capacity of 1 mAh cm^{-2} (Figure 2d). With the deposition current density increasing to 2 mA cm^{-2} with a capacity of 2 mAh cm^{-2}, numerous sharp and vertical dendrites are generated, which shows uneven space electrostatic field distribution on bare Zn surface (Figure 2e).[9a,20] This increased local electric field creates a higher charge region, which encourages more Zn deposition nucleation. Owing to the tip effect, many sharp sheet-like and tip-induced proliferation Zn dendrites are obtained on bare Zn surface when the increment of current density to 3 mA cm^{-2} at a high capacity of 3 mAh cm^{-2}, ultimately resulting in the cell failure (Figure 2f). The MNC@Zn anode surface has negligible changes at current densities of 1, 2, and 3 mA cm^{-2}, which indicates MNC can regulate uniform Zn nucleation and deposition (Figures 2c–e and S14a–c). However, the cross-section SEM images of bare Zn anode surface deliver the increasing dendrite growth (Figures S14d–f). Based on the morphological characterization and electrochemical results, we can conclude that MNC@Zn displays superior Zn dendrites inhibition property due to the more uniform nucleation and lower nucleation overpotential of Zn compared to bare Zn. The uniformly distributed space electric field ensures homogeneous Zn deposition on the surface of Zn foil, thereby obtaining a flat and smooth surface (Figures 2c–e and S14a–c).

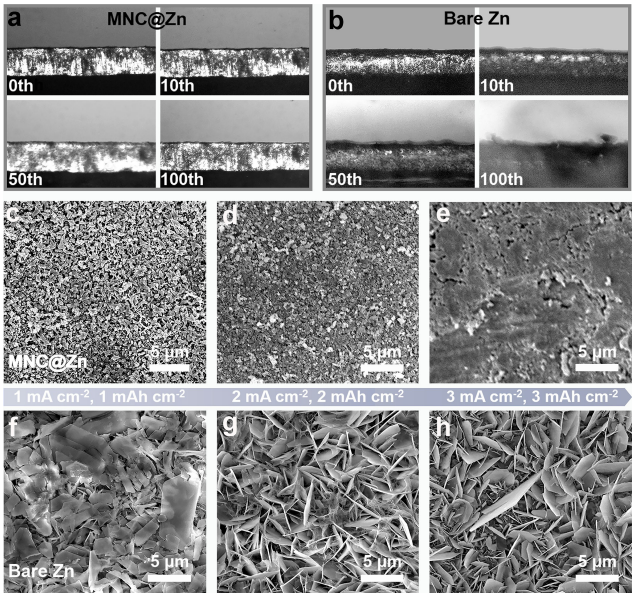

Figure 2. Zn deposition behaviors on MNC@Zn and bare Zn anodes. (a, b) In situ optical observations of the Zn plating process for different cycles at 20 mA cm^{-2} of (a) bare Zn anode, (b) MNC@Zn anode. (c-e) SEM images of the MNC@Zn anode after Zn plating. (c) 1 mA cm^{-2} with a capacity of 1 mAh cm^{-2}. (d) 2 mA cm^{-2} with a capacity of 2 mAh cm^{-2}. (e) 3 mA cm^{-2} with a capacity of 3 mAh cm^{-2}. (f-h) SEM images of bare Zn anode after Zn plating. (f) 1 mAh cm^{-2} with a capacity of 1 mA cm^{-2}. (g) 2 mAh cm^{-2} with a capacity of 2 mA cm^{-2}. (h) 3 mAh cm^{-2} with a capacity of 3 mA cm^{-2}.

Both the SEM observation and optical microscopy tracking manifest that the porous MNC can effectively suppress the formation of Zn dendrites. Due to the desolvation and nucleophilic induction effect, MNC@Zn shows a lower nucleation overpotential of 50.6 mV during the initial deposition stage than bare Zn of 73.6 mV, showing the strong zincophilic ability of MNC. (Figure S15). Furthermore, the effect of MNC on the desolvation effect and inhibition of hydrogen evolution has been employed by linear sweep voltammetry and battery-gas chromatography-mass spectrometry (GC-MS) tests. The hydrogen evolution polarization curves show that the hydrogen evolution current of MNC@Zn electrode is higher than that on the Zn electrode, indicating MNC with integrated micro space electrostatic field can suppress the hydrogen evolution side reactions (Figure S16).[8a] Besides, a GC-MS system with symmetric cell has been connected to ex situ monitor the hydrogen flux at 10 mA cm^{-2} with 5 mAh cm^{-2} (Figure S17). The hydrogen evolution flux of the MNC@Zn symmetric cell delivers the negligible amount of hydrogen evolution no obvious increases (0.0136 mmol h^{-1} cm^{-2} at 3 h) and is >2 orders of magnitude lower than that of bare Zn symmetric cell. Whereas, the hydrogen evolution values of Ti_6@Zn (0.0889 mmol h^{-1} cm^{-2} at 3 h) and Cu_3@Zn (0.0599 mmol h^{-1} cm^{-2} at 3 h) symmetric cells deliver higher than that of MNC@Zn symmetric cell. Base above the results, MNC can effectively inhibit hydrogen evolution and dendrite growth through promoting uniform Zn deposition.

The electrochemical performance of MNC@Zn, Ti_6@Zn, Cu_3@Zn, and the physical mixture@Zn (stands for the physical mixture of Ti_6 and Cu_3 clusters, the mass ratio complies with that of MNC), and bare Zn symmetric cells under various current densities has been examined to further investigate the inhibitory effect of MNC on dendrite growth at virous current densities. Compared to the bare Zn symmetric cell, the MNC@Zn symmetric cell exhibits enhanced long-term plating/stripping cycling stability with smaller voltage fluctuation at 3, 5, 10, or 20 mA cm^{-2} (Figures 3a, 3b, and S18). Impressively, the MNC@Zn symmetric cell displays a more stable and smaller overpotential (≈61.2 mV) of 1200 h for 6000 cycles at 10 mA cm^{-2} than that of the bare Zn symmetric cell with the sharply dropping polarization voltage (≈86 cycles, 102.2 mV), demonstrating the effective inhibition of Zn dendrite growth and elongated plating/stripping cycling stability (Figure 3a). Different from MNC@Zn, the physical mixture symmetric cell presents inevitably voltage fluctuation after 245 h 10 mA cm^{-2}, which can be attributed to the lack in integrated micro space electrostatic field that would lead to the decrease of desolvation effect of the MNC (Figure 3a).[21] Besides, Ti_6, Cu_3 cluster-based symmetric cells present inevitably increased or decreased voltage fluctuation after 165 and 180 h at 10 mA cm^{-2}, respectively (Figures S19 and S20). When the current density increases to 20 mA cm^{-2}, the MNC@Zn can still sustain stable cycling over 1000 h for 10000 cycles with minimal fluctuation (Figure 3b). On the contrary, the polarization voltage for the bare Zn and physical mixture symmetric cells exhibit abruptly decline and randomly oscillates after ≈100 and ≈750 cycles at 20 mA cm^{-2}, respectively (Figure 3b). To confirm the excellent structural integrity and inhibitory effect of the MNC@Zn after 50 cycles at 20 mA cm^{-2}, ex situ morphological evaluation of the MNC@Zn and bare Zn cells have been conducted (Figure S21). Remarkably, the MNC@Zn electrode observes a dense surface devoid of cumulated "dead Zn" or dendritic protrusion, implying MNC can effectively regulating uniform Zn nucleation and deposition (Figures S21a–c).[21a,c] In sharp contrast, SEM morphology with massive Zn dendrites and loosely large blocks can be identified on the surface of the cycled bare Zn anode (Figures S21d–f). The result further demonstrates the efficient induction effect of MNC in guiding dendrite-free Zn deposition, which is ascribed to the uniform space electrostatic field distribution of MNC. To the best of our knowledge, the long-cycle stability (10000 cycles) for the MNC@Zn symmetric cell at 20 mA cm^{-2} outperforms most of the reported anodes of ZMBs that have been described thus far, showing the superiority of this MCOF-Ti_6Cu_3 nanosheet and electrospray in the preparation of Zn coating applications (Figure 3c and Table S1).[4c,8b,12,20,22] The MNC@Zn anode displays outstanding rate performance with steadily raised voltage hysteresis at diverse current densities from 1 to 20 mA cm^{-2}, which outperforms the bare Zn anode and proves the remarkable effect of MNC on reducing the solvation effects to accelerate the deposition kinetic (Figures 3d and S22). Moreover, the voltage hysteresis can be recovered to 46 mV when the current density returns to 1 mA cm^{-2} after 50 cycles, implying a high stability of MNC@Zn. Even at current density of 10 mA cm^{-2} with a high areal capacity of 5 mAh cm^{-2}, the MNC@Zn symmetric cell can still maintain trustworthy voltage stability (Figure S23). Furthermore, the MNC@Cu cell exhibits outstanding cycling stability and a higher average CE of 99.7 % for 200 cycles than that of the bare Cu cell at a high current density of 20 mA cm^{-2} for 5 mAh cm^{-2} (Figure S24).

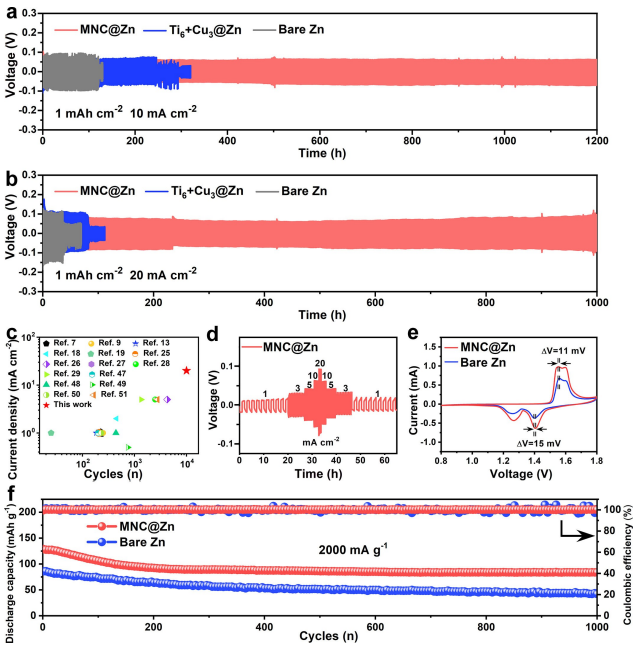

Figure 3. Electrochemical performance of MNC@Zn and bare Zn based batteries. (a) Long-cycling performance of symmetric cells at 10 mA cm^{-2} with a capacity of 1 mAh cm^{-2}. (b) Long-cycling performance of symmetric cells at a current density of 20 mA cm^{-2} with a capacity of 1 mAh cm^{-2}. (c) Comparison of the cycle life of the reported symmetric cells with MNC@Zn. (d) The rate performance of symmetrical cells assembled using MNC@Zn anode at different current densities. (e) CV curves of the MNC@Zn//MnO_2 and Zn//MnO_2 with a MnO_2 mass loading of 1.2 mg cm^{-2}. (f) Cycling performances of the MNC@Zn//MnO_2 and Zn//MnO_2 at 2000 mA g^{-1}.

Inspired by the splendid electrochemical performance of the MNC@Zn anode, full ZMBs composed of commercial MnO_2 cathode and MNC@Zn anode based on aqueous electrolyte (3 M $ZnSO_4$ + 0.1 M $MnSO_4$) have been further assembled and evaluated. The MNC@Zn full battery presents a higher current density by CV curve at 0.1 mV s^{-1} than the bare Zn full battery, indicating a superb electrochemical storage capability (Figure S25). Although the redox peaks of the two cells are comparable, the MNC@Zn/MnO_2 cell has a narrower voltage gap, which indicates a reduced electrochemical polarization (Figure 3e). Additionally, the splendid reversibility of MNC@Zn full cell can also be extrapolated from the similar shapes of the CV curves following the first cycle (Figure S25b). Rate performance of the MNC@Zn//MnO_2 and Zn//MnO_2 full cells are shown in Figure S26. The average discharge capacities of the MNC@Zn//MnO_2 and Zn//MnO_2 full cells are similar, measuring 236.4 and 224.5 mAh g^{-1}, respectively, at a

current density of 0.2 A g^{-1} (Figure S26). With the rise in current density, the MNC@Zn//MnO_2 cell continues to offer excellent discharge capacities of 171.6, 142.7, 127.3, and 95.3 mAh g^{-1} at the current densities of 0.5, 1, 3, and 5 A g^{-1}, respectively. In contrast, the discharge capacity of the Zn/MnO_2 cell rapidly drops to only 60.8 mAh g^{-1} at 5 A g^{-1}. Noteworthy, the MNC@Zn//MnO_2 battery with MnO_2 mass loading of 1.2 mg cm^{-2} produces a high specific capacity of 149.9 mAh g^{-1} after 1000 cycles at 1 A g^{-1} owing to the inhibition of Zn dendrites during cycling (Figure S27). Besides, the MNC@Zn full cell delivers a high initial capacity (252.8 mAh g^{-1}) and still stabilizes at 205.5 mAh g^{-1} after 1000 cycles with a retention rate of 81 % when exposed to an extremely high current density of 2 A g^{-1} (Figure 3f). These results further confirm the superiority of MNC@Zn as the composite Zn anode.

The space electrostatic field distributions at the anode and electrolyte interface can affect the nucleation and deposition of Zn. A theoretical simulation of the finite element method (FEM) has been run using COMSOL to highlight the significance of MNC in regulating the space electrostatic field distribution at the anode and electrolyte interface (Figures 4a–c and S28). Reducing local current density can postpone the nucleation and growth rates of Zn dendrites, in accordance with Sand's time law.[21a,23] The introduced MNC with abundant micro built-in electric field can effectively ensure the charge redistribution that prefers to the Zn^{2+} deposition on the whole electrode rather than local sites, thus guaranteeing a uniform space electrostatic field distribution to achieve a flat and smooth surface (Figures 3c–e, 4a–b and S21a–c). In contrast, the space electrostatic field distribution on the bare Zn surface is inhomogeneous with a distinct intensity gradient during the Zn plating process (Figures 2f–h, 4c, and S21d–f). Such enhanced local space electrostatic field creates a higher charge region, which promotes more local Zn^{2+} deposition nucleation. These small protuberances gradually grow into sharp and large dendritic flakes due to the tip effect, ultimately causing the battery failure (Figure 4c). Based on above results, the computations forcefully demonstrate high affinity and uniform space electrostatic field distributions are essential for MNC in controlling the behavior of Zn nucleation and deposition. Meanwhile, MNC with integrated micro space electrostatic field can prevent the H_2O from direct contact with the Zn electrode and improve desolvation effect of this functional coating. In addition, the electronegative functional groups of the MNC (e.g., Ti–O, Cu–N or C=N groups) maybe also operated as an electrostatic barrier to repulse the incoming SO_4^{2-}.

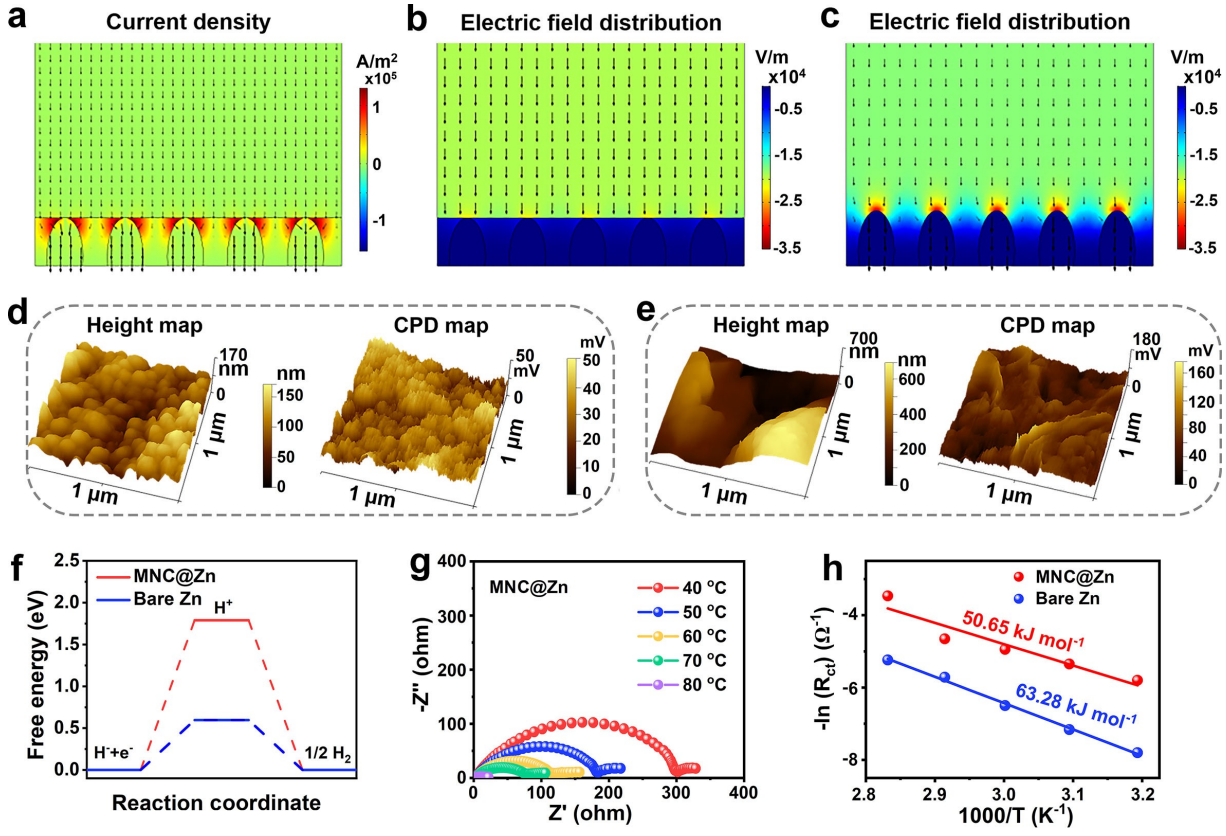

Figure 4. Mechanism investigation of the battery performance for MNC@Zn. (a) COMSOL simulation of MNC@Zn anode. (b) Model of the electric field distributions for MNC@Zn. (c) Model of the electric field distributions for bare Zn. (d) AFM and KPFM images of MNC@Zn anode after 100 cycles. (e) AFM and KPFM images of bare Zn anode after 100 cycles. (f) Gibbs free energy diagram for the hydrogen evolution reaction on MNC@Zn and bare Zn anodes. (g) Nyquist plots of the MNC@Zn symmetric cell at different temperatures. (h) Desolvation energies and corresponding Arrhenius curves of MNC@Zn and bare Zn anodes.

Additionally, the potential distribution and obvious surface morphology of MNC@Zn and bare Zn anodes have been tested by AFM and Kelvin probe force microscopy (KPFM) measurements (Figures 4d and 4e).[21a,23,24] The test results reveal that the MNC@Zn surface has comparatively low height difference and surface potential difference compared to the bare Zn anode surface after 100 cycles at 20 mA cm^{-2}, which is consistent with the results of COMSOL simulation above. According to the calculations, the hydrogen adsorption Gibbs free energy (ΔG_H) on the MNC@Zn interface (1.79 eV) is about twice higher than that of bare Zn (0.60 eV), indicating a low propensity of hydrogen evolution on MNC@Zn (Figure 4f).[5a,24,25] Furthermore, the electrochemical impedance spectroscopy (EIS) consequence at various temperatures ranging from 40 to 80 °C have been evaluated to reflect the transfer kinetic and desolvation ability of Zn^{2+} (Figures 4g, 4h and S29).[5a,24,26] The MNC@Zn symmetric cell shows a much lower charge transfer resistance (R_{ct}) in the Nyquist plots at each corresponding temperature compared to the values for the bare Zn symmetric cell (Figures 4g and S29), further proving an improved capability of the MNC on the charge transfer and Zn deposition kinetic between the electrolyte and electrode. In addition, the calculated activation energy of the MNC@Zn symmetric cell is 50.65 kJ mol^{-1} by Arrhenius equation, which is lower than that of the bare Zn symmetric cell (63.28 kJ mol^{-1}, Figure 4h). This indicates that the MNC can effectively decrease the desolvation energy barrier during the charge transfer process, leading to improved Zn^{2+} kinetic behavior during the deposition/stripping process.[5a,26]

To justify the influence of MNC during the Zn deposition process, the Zn adsorption energy and diffusion energy barrier have been examined by density functional theory (DFT) calculation. Note that all the theoretical calculations use Zn metal as the reference. We firstly carry out the absorption energies of Zn on MNC and Zn (001), owing to that Zn (001) is the most stable surface and generally applied as calculation model by many ZMBs related references.[18] Compared to the bare Zn, the calculated adsorption energy of Zn on the MNC surface is substantially stronger, demonstrating that the better zincophilicity of MNC can result in easier Zn desolvation (Figures 5a and S30a). Specifically, there exists a stronger interaction between Ti–O site of MNC and Zn (absorption energy, −2.14 eV), whereas the absorption energy between Zn and Zn (001) is only −0.64 eV, inhibiting the irregular diffusion of Zn^{2+} and the growth of Zn dendrites (Figure S30b). Beyond that, the most stable configurations for MNC with Zn adsorption are shown in differential charge density and results show that the MNC can effectively impede the "tip-effect-induced" Zn dendrites seen on the bare Zn by adhering and immobilizing a certain quantity of Zn during the Zn plating process to reduce interfacial concentration gradients (Figures 5b and S31). In addition, we also investigated the diffusion energy barrier of Zn^{2+} migration between adjacent energy minima on Zn (001) and MNC@Zn surfaces (Figure S32). MNC@Zn possesses a higher activation energy of 0.062 eV to hinder the migration and

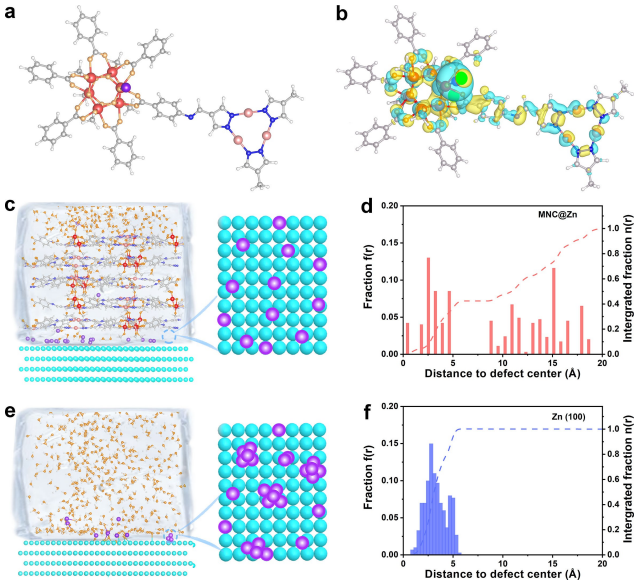

Figure 5. Theoretical calculation uncovering the impact of MNC@Zn deposition behavior. (a) The calculation model of Zn absorbed on MNC (purple balls present the adsorbed Zn). (b) Charge density difference of the MNC with Zn adsorption. (c) The schematic diagrams of MD simulations of Zn^{2+} deposition on the MNC@Zn anode surface (only Zn^{2+} in electrolyte and Zn^{2+} deposited on the surface are shown for clearer visualization). (d) Corresponding RDFs plots of Zn^{2+} deposited on the surface of MNC@Zn. (e) The schematic diagrams of MD simulations of Zn^{2+} deposition on the bare Zn surface (only Zn^{2+} in electrolyte and Zn^{2+} deposited on the surface with coordinated water molecules are shown for clearer visualization). (f) Corresponding RDFs plots of Zn^{2+} deposited on the bare Zn surface.

subsequent agglomeration of Zn^{2+} into Zn dendrites (Figure S32b). As a result, MNC acts as a buffer or regulating layer to homogenize the Zn^{2+} flux or reduce the diffusion rate of Zn^{2+}, which guides the dendrite-free Zn deposition. Contrarily, Zn^{2+} on Zn (001) surface has an activation energy of only 0.02 eV, indicating that Zn^{2+} diffusion there is instantaneous, favoring inhomogeneous mossy-like Zn deposition (Figure S32).[20,27]

Moreover, molecular dynamics (MD) simulations of MNC@Zn and bare Zn anodes have been carried out to further explain the positive effect of the MNC on regulating the Zn dissolution/precipitation behavior on ZMBs. The calculation models are constructed using the finite clusters structures of MCOF-Ti_6Cu_3 (Figures S33–S35). Therefore, MNC@Zn anode can be more beneficial to eliminate the dendritic interference due to the higher Zn adsorption energy and surface diffusion barrier than bare Zn anode. The DFT based high-dimensional neutral network potential (HDNNPs) is conducted to simulate the Zn ions desolvation and transport dynamics under space electrostatic field driven penetration mechanism in aqueous electrolyte (Videos S1 and S2).[28] The result of MNC@Zn shows a reduction of active water around Zn^{2+} that moving to Zn (001) surface as the quasi-free state in aqueous electrolyte, suggesting a higher activity lead to facilitate the homogeneous nucleation and growth on Zn (001) surface during the Zn plating (Video S1). In contrast, bare Zn anode exhibits that the

difficulty of water shell stripping and the decrease of Zn activity, which makes Zn preferentially adsorbed at the hump-sites for aggregation, thus evolving into generating Zn dendrites (Video S2). Hence, the significant role of MNC in inhibition of Zn dendrite growth. The MD simulation of Zn ions of MNC displays a one magnitude higher Zn^{2+} diffusion coefficient value ($5.699E^{-3}$ A^2/fs^{-1}) than that of the aqueous electrolyte ($0.703E^{-4}$ A^2/fs^{-1}), which is consistent with experimental results (Figures 4h, S36 and Video S3). Based on the above results, MNC can efficient promote the kinetic of ion diffusion and prevent the growth of Zn dendrites to achieve superior electrochemical performance. In the MD simulations, Zn^{2+} deposit on both bare Zn and MNC@Zn surfaces driven by an applied space electrostatic field. Interestingly, Zn preferentially and evenly deposit beneath the whole surface Zn substrate in the MNC@Zn model (Figure 5c and Video S1), which is opposed to results of bare Zn model that mainly concentrates on the defect region (Figure 5e and Video S2). Beyond that, the associated radial distribution functions (RDFs) and the amount of Zn ions deposited on the both MNC@Zn and bare Zn model surfaces have been also analyzed by the time evolution of the quantity of Zn ions coupled to the anodes (Figures 5d and 5f).[22d] Compared to the value in the bare Zn model, the deposited Zn^{2+} amount has been boosted evidently with the use of MNC in the MNC@Zn model, demonstrating that MNC obviously accelerates the Zn^{2+} deposition dynamics on the beneath the Zn foil surface during the charging process. Compared to bare Zn, the reduced f(r) value of MNC@Zn indicates that the probability of zinc ions binding to water molecules is decreased, proving the MNC can modulate the solvation structure of Zn^{2+} ions by immobilizing the free water molecules. In addition, the MNC@Zn model simultaneously displays a broader distribution of Zn^{2+} when compared to that of bare Zn model, further demonstrates the much more uniform Zn^{2+} deposition in the MNC@Zn model.

Conclusion

In conclusion, a hetero-metallic cluster MNC with integrated micro space electrostatic field has been successfully designed and applied as functional interfacial coating for ZMBs anode by large-scale electrospray fabrication. Remarkably, it can achieve the scalable fabrication of MNC@Zn with $>10000\,cm^2$ in a batch-experiment. The hetero-metallic cluster in MNC can generate integrated micro space electrostatic field to accelerate the desolvation of hydrated ions and improve the deposition kinetics of Zn^{2+}, thus inhibiting the growth of Zn dendrites and hydrogen to improve the lifespan of Zn anode as proved by the experimental characterizations and theoretical calculations. Notably, thus-obtained MNC@Zn symmetric cell presents an ultralow overpotential (≈ 72.8 mV) for 10000 cycles at $1\,mAh\,cm^{-2}$ with $20\,mA\,cm^{-2}$, which is far superior to bare Zn or monomers based symmetric cells and represented to be optimal in COF based coatings. This is the first case of porous crystalline material based ZMBs anode coating with integrated micro space electrostatic field that can be scalable production, which would promote the development of high-performance ZMBs.

Acknowledgements

This work was financially supported by the NSFC (Grants 21871141, 21871142, 21901122, 22071109, 22105080 and 22171139).

Conflict of Interest

The authors declare no conflict of interest.

Data Availability Statement

The data that support the findings of this study are available from the corresponding author upon reasonable request.

Keywords: Hetero-Metallic Cluster · Metal-Covalent Organic Frameworks · Micro Space Electrostatic Field · Suppression the Zn Dendrite Growth

[1] a) N. Kittner, F. Lill, D. M. Kammen, *Nat. Energy* **2017**, *2*, 17125; b) S. Liu, R. Zhang, J. Mao, Y. Zhao, Q. Cai, Z. Guo, *Sci. Adv.* **2022**, *8*, eabn5097.

[2] a) R. F. Service, *Science* **2021**, *372*, 890–891; b) H. Zhang, Q. Liu, Y. Fang, C. Teng, X. Liu, P. Fang, Y. Tong, X. Lu, *Adv. Mater.* **2019**, *31*, 1904948.

[3] a) Y. Liang, Y. Jing, S. Gheytani, K. Y. Lee, P. Liu, A. Facchetti, Y. Yao, *Nat. Mater.* **2017**, *16*, 841–848; b) P. Canepa, G. S. Gautam, D. C. Hannah, R. Malik, M. Liu, K. G. Gallagher, K. A. Persson, G. Ceder, *Chem. Rev.* **2017**, *117*, 4287–4341.

[4] a) P. X. Sun, Z. Cao, Y. X. Zeng, W. W. Xie, N. W. Li, D. Luan, S. Yang, L. Yu, X. W. Lou, *Angew. Chem. Int. Ed.* **2022**, *61*, e202115649; *Angew. Chem.* **2022**, *134*, e202115649; b) Q. Zhang, J. Luan, L. Fu, S. Wu, Y. Tang, X. Ji, H. Wang, *Angew. Chem. Int. Ed.* **2019**, *58*, 15841–15847; *Angew. Chem.* **2019**, *131*, 15988–15994; c) Q. Xu, W. Zhou, T. Xin, Z. Zheng, X. Yuan, J. Liu, *J. Mater. Chem. A* **2022**, *10*, 12247–12257.

[5] a) S. Jiao, J. Fu, M. Wu, T. Hua, H. Hu, *ACS Nano* **2022**, *16*, 1013–1024; b) P. Liu, B. Chen, C. Liang, W. Yao, Y. Cui, S. Hu, P. Zou, H. Zhang, H. J. Fan, C. Yang, *Adv. Mater.* **2021**, *33*, 2007377; c) H. Dai, J. Dong, M. Wu, Q. Hu, D. Wang, L. Zuin, N. Chen, C. Lai, G. Zhang, S. Sun, *Angew. Chem. Int. Ed.* **2021**, *60*, 19852–19859; *Angew. Chem.* **2021**, *133*, 20005–20012.

[6] a) H. Yu, Y. Zeng, N. W. Li, D. Luan, L. Yu, X. W. D. Lou, *Sci. Adv.* **2022**, *8*, eabm5766; b) J. F. Parker, C. N. Chervin, I. R. Pala, M. Machler, M. F. Burz, J. W. Long, D. R. Rolison, *Science* **2017**, *356*, 415–418.

[7] a) J. Hao, L. Yuan, C. Ye, D. Chao, K. Davey, Z. Guo, S.-Z. Qiao, *Angew. Chem. Int. Ed.* **2021**, *60*, 7366–7375; *Angew. Chem.* **2021**, *133*, 7442–7451; b) D. Chao, W. Zhou, F. Xie, C. Ye, H. Li, M. Jaroniec, S.-Z. Qiao, *Sci. Adv.* **2020**, *6*, eaba4098.

[8] a) L. Wang, W. Huang, W. Guo, Z. H. Guo, C. Chang, L. Gao, X. Pu, *Adv. Funct. Mater.* **2022**, *32*, 2108533; b) Y. Zeng, P. X. Sun, Z. Pei, Q. Jin, X. Zhang, L. Yu, X. W. Lou, *Adv. Mater.* **2022**, *34*, 2200342.

[9] a) Z. Wang, J. Huang, Z. Guo, X. Dong, Y. Liu, Y. Wang, Y. Xia, *Joule* **2019**, *3*, 1289–1300; b) M. Zhu, J. Hu, Q. Lu, H. Dong, D. D. Karnaushenko, C. Becker, D. Karnaushenko, Y. Li, H. Tang, Z. Qu, J. Ge, O. G. Schmidt, *Adv. Mater.* **2021**, *33*, 2007497.

[10] N. Zhang, S. Huang, Z. Yuan, J. Zhu, Z. Zhao, Z. Niu, *Angew. Chem. Int. Ed.* **2021**, *60*, 2861–2865; *Angew. Chem.* **2021**, *133*, 2897–2901.

[11] a) X. Zhao, P. Pachfule, A. Thomas, *Chem. Soc. Rev.* **2021**, *50*, 6871–6913; b) N. Keller, T. Bein, *Chem. Soc. Rev.* **2021**, *50*, 1813–1845; c) K. Geng, T. He, R. Liu, S. Dalapati, K. T. Tan, Z. Li, S. Tao, Y. Gong, Q. Jiang, D. Jiang, *Chem. Rev.* **2020**, *120*, 8814–8933.

[12] a) J. H. Park, M. J. Kwak, C. Hwang, K. N. Kang, N. Liu, J. H. Jang, B. A. Grzybowski, *Adv. Mater.* **2021**, *33*, 2101726; b) Z. Zhao, R. Wang, C. Peng, W. Chen, T. Wu, B. Hu, W. Weng, Y. Yao, J. Zeng, Z. Chen, P. Liu, Y. Liu, G. Li, J. Guo, H. Lu, Z. Guo, *Nat. Commun.* **2021**, *12*, 6606; c) C. Guo, J. Zhou, Y. Chen, H. Zhuang, Q. Li, J. Li, X. Tian, Y. Zhang, X. Yao, Y. Chen, S.-L. Li, Y.-Q. Lan, *Angew. Chem. Int. Ed.* **2022**, *61*, e202210871; *Angew. Chem.* **2022**, *134*, e202210871; d) J. Zhao, Y. Ying, G. Wang, K. Hu, Y. D. Yuan, H. Ye, Z. Liu, J. Y. Lee, D. Zhao, *Energy Storage Mater.* **2022**, *48*, 82–89; e) X. Hu, Z. Lin, S. Wang, G. Zhang, S. Lin, T. Huang, R. Chen, L.-H. Chung, J. He, *ACS Appl. Energy Mater.* **2022**, *5*, 3715–3723; f) H. Wang, S. Zhao, Y. Liu, R. Yao, X. Wang, Y. Cao, D. Ma, M. Zou, A. Cao, X. Feng, B. Wang, *Nat. Commun.* **2019**, *10*, 4204.

[13] a) M. S. Denny Jr., S. M. Cohen, *Angew. Chem. Int. Ed.* **2015**, *54*, 9029–9032; *Angew. Chem.* **2015**, *127*, 9157–9160; b) S. Xia, L. Song, N. Hohn, K. Wang, S. Grott, M. Opel, M. Schwartzkopf, S. V. Roth, P. Mueller-Buschbaum, *Adv. Funct. Mater.* **2019**, *29*, 1808427; c) A. M. Evans, N. P. Bradshaw, B. Litchfield, M. J. Strauss, B. Seckman, M. R. Ryder, I. Castano, C. Gilmore, N. C. Gianneschi, C. R. Mulzer, M. C. Hersam, W. R. Dichtel, *Adv. Mater.* **2020**, *32*, 2004205.

[14] a) Z. Chen, R. Wang, T. Ma, J.-L. Wang, Y. Duan, Z.-Z. Dai, J. Xu, H.-J. Wang, J. Yuan, H.-L. Jiang, Y.-W. Yin, X.-G. Li, M.-R. Gao, S.-H. Yu, *Angew. Chem. Int. Ed.* **2021**, *60*, 14124–14130; *Angew. Chem.* **2021**, *133*, 14243–14249; b) A. Knebel, J. Caro, *Nat. Nanotechnol.* **2022**, *17*, 911–923.

[15] Z.-F. Cai, G. Zhan, L. Daukiya, S. Eyley, W. Thielemans, K. Severin, S. De Feyter, *J. Am. Chem. Soc.* **2019**, *141*, 11404–11408.

[16] a) J. Zhou, J. Li, L. Kan, L. Zhang, Q. Huang, Y. Yan, Y. Chen, J. Liu, S.-L. Li, Y.-Q. Lan, *Nat. Commun.* **2022**, *13*, 4681; b) M. Lu, J. Liu, Q. Li, M. Zhang, M. Liu, J.-L. Wang, D.-Q. Yuan, Y.-Q. Lan, *Angew. Chem. Int. Ed.* **2019**, *58*, 12392–12397; *Angew. Chem.* **2019**, *131*, 12522–12527.

[17] Z.-W. Wang, Y.-Z. Shi, C. Liu, Y.-Y. Kang, L. Wu, *Appl. Catal. B* **2022**, *301*, 120803.

[18] a) X. Li, J. Wang, F. Xue, Y. Wu, H. Xu, T. Yi, Q. Li, *Angew. Chem. Int. Ed.* **2021**, *60*, 2534–2540; *Angew. Chem.* **2021**, *133*, 2564–2570; b) Y. Yang, X. Zhang, S. Kanchanakungwankul, Z. Lu, H. Noh, Z. H. Syed, O. K. Farha, D. G. Truhlar, J. T. Hupp, *J. Am. Chem. Soc.* **2020**, *142*, 21169–21177.

[19] P. Xue, C. Guo, N. Wang, K. Zhu, S. Jing, S. Kong, X. Zhang, L. Li, H. P. Li, Y. Feng, W. Gong, Q. Li, *Adv. Funct. Mater.* **2021**, *31*, 2106417.

[20] X. Liu, F. Yang, W. Xu, Y. Zeng, J. He, X. Lu, *Adv. Sci.* **2020**, *7*, 2002173.

[21] a) H. Li, C. Guo, T. Zhang, P. Xue, R. Zhao, W. Zhou, W. Li, A. Elzatahry, D. Zhao, D. Chao, *Nano Lett.* **2022**, *22*, 4223–4231; b) H. Yan, S. Li, Y. Nan, S. Yang, B. Li, *Adv. Energy Mater.* **2021**, *11*, 2100186; c) Q. Li, A. Chen, D. Wang, Z. Pe, C. Zhi, *Joule* **2022**, *6*, 273–279.

[22] a) R. Yuksel, O. Buyukcakir, W. K. Seong, R. S. Ruoff, *Adv. Energy Mater.* **2020**, *10*, 1904215; b) G. Li, X. Wang, S. Lv, J. Wang, X. Dong, D. Liu, *Chem. Eng. J.* **2022**, *450*, 138116; c) H. Yang, Z. Chang, Y. Qiao, H. Deng, X. Mu, P. He, H. Zhou, *Angew. Chem. Int. Ed.* **2020**, *59*, 9377–9381; *Angew. Chem.* **2020**, *132*, 9463–9467; d) Q. Zhang, J. Luan, X. Huang, Q. Wang, D. Sun, Y. Tang, X. Ji, H. Wang, *Nat. Commun.* **2020**, *11*, 3961; e) Q. Zhang, Y. Ma, Y. Lu, X. Zhou, L. Lin, L. Li, Z. Yan, Q. Zhao, K. Zhang, J. Chen, *Angew. Chem. Int. Ed.* **2021**, *60*, 23357–23364; *Angew. Chem.* **2021**, *133*, 23545–23552.

[23] a) P. Xue, C. Guo, L. Li, H. P. Li, D. Luo, L. C. Tan, Z. W. Chen, *Adv. Mater.* **2022**, *34*, 2110047; b) Y. Fang, S. L. Zhang, Z.-P. Wu, D. Luan, X. W. Lou, *Sci. Adv.* **2021**, *7*, eabg3626; c) X. Xiao, Y. Zhou, X. Zhao, G. Chen, Z. Liu, Z. Wang, C. Lu, M. Hu, A. Nashalian, S. Shen, K. Xie, W. Yang, Y. Gong, W. Ding, P. Servati, C. Han, S. X. Dou, W. Li, J. Chen, *Sci. Adv.* **2021**, *7*, eabl3742.

[24] J.-L. Yang, J. Li, J.-W. Zhao, K. Liu, P. Yang, H. J. Fan, *Adv. Mater.* **2022**, *34*, 2202382.

[25] L. Ma, Q. Li, Y. Ying, F. Ma, S. Chen, Y. Li, H. Huang, C. Zhi, *Adv. Mater.* **2021**, *33*, 2007406.

[26] X. Xie, S. Liang, J. Gao, S. Guo, J. Guo, C. Wang, G. Xu, X. Wu, G. Chen, J. Zhou, *Energy Environ. Sci.* **2020**, *13*, 503–510.

[27] M. S. Kim Deepika, S. H. Lee, M.-S. Kim, J.-H. Ryu, K.-R. Lee, L. A. Archer, W. I. Cho, *Sci. Adv.* **2019**, *5*, eaax5587.

[28] J. Behler, *Angew. Chem. Int. Ed.* **2017**, *56*, 12828–12840; *Angew. Chem.* **2017**, *129*, 13006–13020.

Manuscript received: January 3, 2023
Accepted manuscript online: January 20, 2023
Version of record online: ■■, ■■

Research Articles

Aqueous Zn-Ion Batteries

C. Guo, J. Zhou, Y. Chen, H. Zhuang, J. Li, J. Huang, Y. Zhang, Y. Chen,* S.-L. Li, Y.-Q. Lan* _____ e202300125

Integrated Micro Space Electrostatic Field in Aqueous Zn-Ion Battery: Scalable Electrospray Fabrication of Porous Crystalline Anode Coating

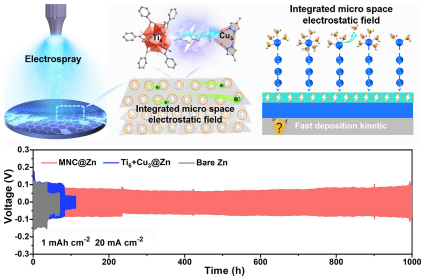

Electrospray has been applied for scalable fabrication (>10000 cm^2 in a batch-experiment) of hetero-metallic cluster covalent-organic-frameworks (MCOF-Ti_6Cu_3) nanosheet-coating (MNC) with integrated micro space electrostatic field for ZMBs anode protection.